Particle Transport and Fluctuation Characteristics around the Neoclassically Optimized Configuration in LHD

Kenji TANAKA, Clive MICHAEL, Leonid N. VYACHESLAVOV[1], Masayuki YOKOYAMA,
Sadayoshi MURAKAMI[2], Arimitsu WAKASA[3], Hidenobu TAKENAGA[4], Katsunori MURAOKA[5],
Kazuo KAWAHATA, Tokihiko TOKUZAWA, Tsuyoshi AKIYAMA, Katsumi IDA, Mikiro
YOSHINUMA, Ichihiro YAMADA, Kazumichi NARIHARA, Hiroshi YAMADA
and the LHD Experimental Group

National Institute for Fusion Science,322-6 Oroshi-cho, Toki 509-5292, Japan
[1]*Budker Institute of Nuclear Physics, 630090 Nobosibirsk, Russia*
[2]*Department of Nuclear Engineering, Kyoto University, Kyoto 606-8501, Japan*
[3]*Graduate School of Engineering, Hokkaido University, Sapporo 060-8628, Japan*
[4]*Japan Atomic Energy Agency, 801-1, Mukoyama, Naka 311-0193, Japan*
[5]*School of Engineering, Chubu University, Kasugai 487-8501, Japan*

Density profiles in LHD were measured and particle transport coefficients were estimated from density modulation experiments in LHD. The dataset used in this article included a wide range of discharge conditions, e.g., for different heating powers, magnetic axes, and toroidal magnetic fields scanned to cover wide regions for neoclassical transport. The minimized neoclassical transport configuration in the dataset (R_{ax} = 3.5 m, B_t = 2.83 T) showed peaked density profiles, and its peaking factors increased gradually with decreasing collisionality. These results are similar to those observed in tokamaks. At some other configurations, peaking factors were reduced with decreasing collisionality and a larger contribution of neoclassical transport produced hollow density profiles. Comparison between neoclassically and experimentally estimated particle diffusivities showed different minimum conditions. This suggests that the condition for neoclassical optimization is not the same as that for anomalous optimization. A clear difference in spatial profiles of turbulence was observed between hollow and peaked density profiles. A major part of the fluctuations existed in the unstable region of the linear growth rate of the ion temperature gradient mode and trapped electron mode.

1. Introduction

Optimization of magnetic configuration for reducing energy and particle transport is an important issue for studies in stellarator/heliotron devices. Magnetic properties can be changed by scanning magnetic axis positions (R_{ax}) in LHD. Therefore, a scan of R_{ax} is an effective way to conduct systematic studies on the effects of magnetic configuration on transport. A study was carried out to find the optimum configuration for reducing neoclassical transport over R_{ax} = 3.5 ~ 3.75 m using the DCOM code, and it was found that neoclassical transport is minimum at R_{ax} = 3.5 m in the plateau regime and at R_{ax} = 3.53 m in the $1/\nu$ regime [1]. On the other hand, it was experimentally observed that the effective helical ripple, which is an influential parameter of neoclassical transport in the $1/\nu$ regime, played an important role on global energy confinement [2]. Comparative studies among different machines show that smaller effec-

tive helical ripple configurations showed enhancement in global energy confinement compared with the international stellarator scaling 2005 [2]. This suggests that neoclassical optimization may also reduce anomalous transport because most transport in the data set of Ref. [2] was dominated by anomalous transport. In our previous work, systematic studies of particle transport and fluctuation properties were carried out over R_{ax} = 3.6, 3.75, and 3.9 m at around 1.5 T and R_{ax} = 3 6 m at 2.75 and 2.8 T [3, 4]. Particle diffusion was found to be anomalous and smaller at more inwardly shifted configurations. At the same time, a smaller edge fluctuation level was also observed. Density profiles were hollow in many cases of discharge conditions, and became peaked at higher magnetic fields and collisionality. When density profiles were hollow, particle convection was comparable with that from the neoclassical prediction.

In this article, additional analyses are reported that have been carried out to get more insight into the dependence of configuration on particle transport. We fo-

cused on linkages between neoclassical optimization and anomalous optimization, and the effect of magnetic field strengths.

2. Experimental Results and Discussion

2.1 General characteristics of density profiles in LHD

Figure 1 shows electron temperature (T_e) and electron density (n_e) profiles under different discharge conditions. Density profiles were measured using a multi-channel far-infrared interferometer [5] and a CO_2 laser interferometer [6]. Electron temperature profiles were measured by YAG Thomson scattering [7]. As seen in these figures, density profiles were different depending on discharge conditions. This is a clear contrast to tokamak density profiles, which are peaked in most cases [8,9]. In LHD, the density profile changes from peaked to hollow with an increase in heating power, as shown in Fig. 1 (b). These changes of density profiles can be explained by the increase in neoclassical

outward convection with decreasing collisionality [3].

Figure 1 (c) and (d) shows the effects of magnetic axis positions. Even for identical T_e profiles, at an inwardly shifted configuration of $R_{ax} = 3.50$ m, the density profile peaked while at an outwardly shifted configuration of $R_{ax} = 3.75$ m, the density profile was hollow. This can be explained by the enhanced outward neoclassical convection at a more outwardly shifted configuration [3].

Figures 1 (e) and (f) show T_e and n_e profiles under different toroidal magnetic field strengths (B_t) for almost the same T_e profiles at the same configuration ($R_{ax} = 3.6$ m). At a lower magnetic field, the density profile was more hollow. Thus, the magnetic field strength can also affect density profiles.

In order to understand these configurations and magnetic field dependences of density profiles more precisely, dependences of the peaking factor of density profiles were studied and are summarized in Figs. 2-4. Here, the peaking factor was defined as the ratio of the density at ρ (normalized radius) = 0.2 against the volume averaged density. The volume averaged density was calculated within the last closed flux surface. Data of JT60-U are also presented for comparison.

The data in Figs. 2-4 are from NBI heated plasmas. However, particle fueling from the NBI was found to have no effect on density peaking factors in both JT-60U and LHD [3,4,8]. Thus, variations of density profiles are due to the difference of transport.

Figure 2 (a) shows dependences of density peaking factors of JT60-U and LHD on ν_b^*, which is the electron-ion collision frequency normalized using the collision frequency at the plateau-banana boundary, and can be written as follows:

$$\nu_b^* = \nu_{ei}/(\varepsilon_t^{3/2} v_T/qR) \qquad (1)$$

where ε_t is an inverse aspect ratio, v_T is an electron thermal velocity, q is the safety factor, and R is a major radius. The value of ε_t at $\rho = 0.5$ was defined as that at $0.5a/R$, where a is the averaged minor radius of the last closed flux surface.
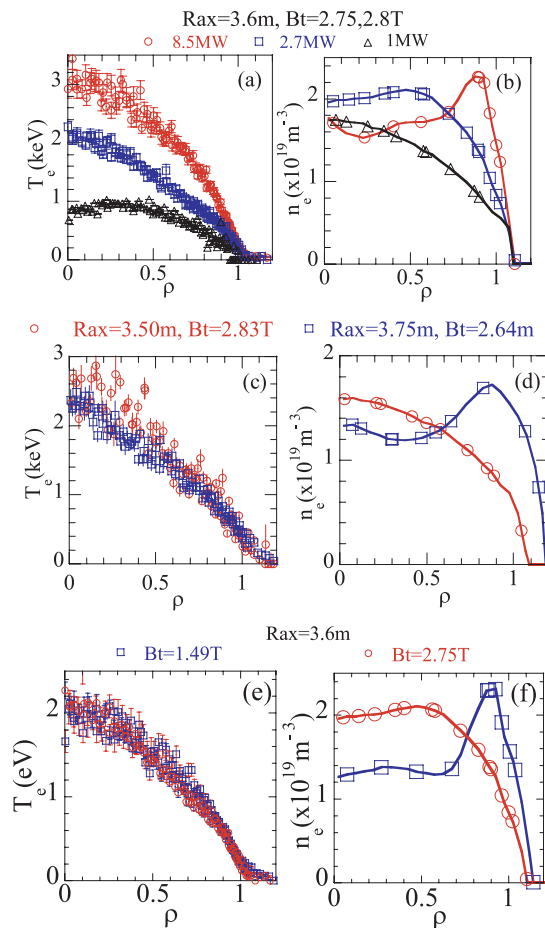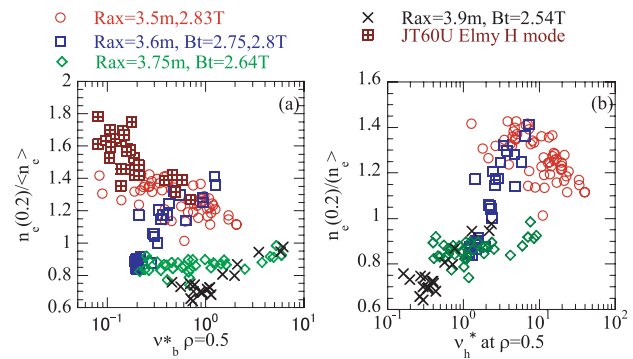

Fig. 1 Comparison of (a), (c), (e) T_e and (b), (d), (f) n_e profiles under different conditions. (a), (b) Different NBI powers at $R_{ax} = 3.6$ m. (c), (d) Different magnetic configurations at $R_{ax} = 3.5$ and 3.75 m. (e), (f) Different magnetic fields at $R_{ax} = 3.6$ m.

Fig. 2 Collisionality dependence of density peaking factors: (a) comparison between LHD and JT-60U, and (b) comparison between four configurations of LHD at high fields (B_t = 2.54-2.80 T)
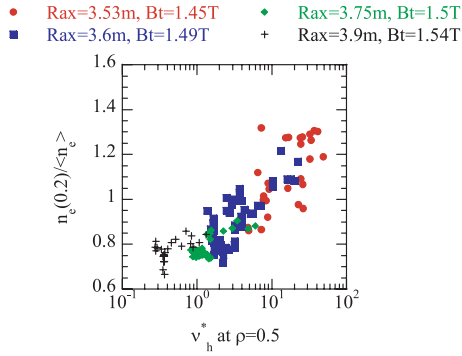
Fig. 3 Collisionality dependence of density peaking factors among four configurations of LHD at lower fields (B_t = 1.45-1.54 T)
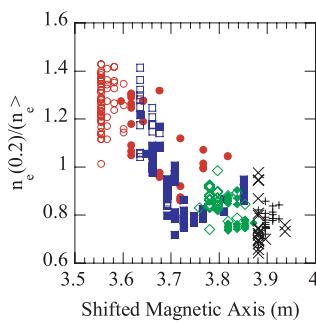

Fig. 4 Dependences of density peaking factors on shifted magnetic axes. Symbols are the same as in Figs. 2 and 3.

Figure 2 (b) shows dependences of density peaking factors of LHD on ν_h^*, which is defined as follows:

$$\nu_h^* = \nu_{ei}/(\varepsilon_{eff}^{3/2}\upsilon_T/qR) \qquad (2)$$

Here, ε_{eff} is an effective helical ripple, which has been introduced to represent multiple helicity and is defined as [10]

$$\varepsilon_{eff} = \left(\frac{9\sqrt{2}}{16}\frac{\nu}{\upsilon_d^2}D\right)^{2/3} \qquad (3)$$

Here, ν, υ_d, and D are the collision frequency, drift velocity, and particle diffusivity in the enhanced helical ripple-trapped region, which is the so-called $1/\nu$ region, respectively. At the upper boundary of the $1/\nu$ region, ν_h^* approaches unity. This dependence on ν_h^* is convenient to understand experimental regimes in neoclassical transport. The finite beta effects were included in the estimation of ε_{eff} [11].

JT60-U data in Fig. 2 (a) represent density profiles for cases of negligible neoclassical transport. The data are taken from the database of the Elmy H-mode [8]. The density profiles of JT60-U were measured using YAG Thomson scattering. In JT-60U, density peaking factors increased with decreasing ν_b^*. This has been widely observed in tokamaks [8, 9]. One of the possible interpretations of this observation is an enhanced turbulence-driven

inward pinch in the low collision regime. The growth rate of the ion temperature gradient (ITG) mode in tokamaks increases with decreasing collisionality [9]. JT60-U data in Fig. 2 (a) were in the ITG unstable region, because the ion temperature gradient mode parameter, defined as $\eta_i = L_{n_e}/L_{T_i}$ where $L_{n_e} = (-\nabla n_e/n_e)^{-1}$ and $L_{T_i} = (-\nabla T_i/T_i)^{-1}$, was larger than unity ($\eta_i > 1$) [8]. Therefore, JT60-U data also support the role of turbulence on peaked density profiles

As shown in Fig. 2 (a), the density profiles for R_{ax} = 3.5 m in B_t = 2.83 T are peaked while those for R_{ax} = 3.6 m in B_t = 2.75 and 2.80 T change from peaked to hollow, and the profiles for R_{ax} = 3.75 m in B_t = 2.64 T and R_{ax} = 3.9 m in B_t = 2.54 T were hollow. Density peaking factors gradually increased with decreasing ν_b^* only at R_{ax} = 3.5 m in B_t = 2.83 T. At R_{ax} = 3.6 m in B_t = 2.75 and 2.8 T and R_{ax} = 3.9 m in B_t = 2.54 T, density peaking factors show a tendency opposite to JT60-U for the dependence on ν_b^*. As mentioned above, in tokamaks, an increase of the density peaking factor can be due to the increase of turbulence-driven inward pinch. The data of R_{ax} = 3.5 m 2.83 T showed similar tendency to JT60-U data. Therefore, we may assume that the turbulence-driven inward pinch causes peaked density profiles for R_{ax} = 3.5 m in B_t = 2.83 T.

As shown in Fig. 2 (b), the density peaking factor shows a clear dependence on ν_h^*. At a more outward shift configuration, ε_{eff} becomes larger, so for the same ν_{ei}, ν_h^* becomes smaller. At smaller ν_h^*, the contribution of neoclassical transport is larger, the peaking factor decreases, and the density profile becomes more hollow. This is well explained by the increase in neoclassical outward convection [3]. The linear growth rate becomes smaller at the hollow density profile compared with the peaked density profile [12]. At a more outward configuration, the neoclassical contribution becomes larger and anomalous contribution becomes smaller, and vice versa. Figure 2 (b) shows that larger neoclassical transport at a more outwardly shifted configuration results in a hollow density profile, and larger anomalous transport at a more inwardly shifted configuration results in a peaked density profile.

It should be noted that that for R_{ax} = 3.75 in B_t = 2.64 T, density peaking factors were almost constant for variations of ν_b^* and ν_h^*, as shown in Fig. 2 (a) and (b). A constant peaking factor indicates that values of $(aV)/D$ were kept constant, where a is the averaged minor radius, V is the convection velocity, and D is the diffusion coefficient. The diffusion coefficient increased and convection velocity increased outwardly with decreasing collisionality [3]. Although, the density profiles were constant, the particle transport was not.

Figure 3 shows dependence on ν_h^* at lower magnetic fields (R_{ax} = 3.53 m in B_t = 1.45 T, R_{ax} = 3.6 m in B_t = 1.49 T, R_{ax} = 3.75 m in B_t = 1.50 T, and R_{ax} = 3.9 m in B_t = 1.54 T). Clearer dependence on ν_h^* was observed. Also, density peaking factors are smaller at lower fields. A pos-

sible interpretation of this trend is due to the larger Shavranov shift at lower fields. The lower magnetic field introduces higher β and larger Shavranov shifts. The Shavranov shift gives the same effect as outwardly external plasma movement due to the externally applied vertical field.

Figure 4 shows the dependence of density peaking factors on the shifted magnetic axes. Figure 4 includes both low and high field data. Here, the plasma axis shift was estimated from the Abel inversion of an interferometer [5]. Decreases in peaking factors with increases in the shifted magnetic axes are clearly seen. For example, the density peaking factor at R_{ax} = 3.53 m in 1.45 T with a high heating power (low collisionality) is close to that at R_{ax} = 3.75 m in 2.64 T with a low heating power (high collisionality). This indicates that an outward-shift of a magnetic axis due to the Shavranov shift is equivalent to an outward position of the magnetic axis by the external vertical field. Energy transport from the power balance analysis shows a similar tendency [13].

2.2 Parameter dependence of particle transport coefficients for R_{ax} = 3.5 m and R_{ax} = 3.6 m

As described in the previous section, a magnetic axis position is an important parameter in determining density profiles in LHD. The effect of magnetic fields is understood to change the magnetic axis position due to the Shavranov shift. There is a clear difference of collisionality dependence between R_{ax} = 3.5 m in B_t = 2.83 T, and R_{ax} = 3.6 m in B_t = 2.75 T and 2.80 T as shown in Fig. 2 (a). This indicates that there is a clear difference of transport mechanism between the two cases. In this section, characteristics of particle transport and their parameter dependence are compared between the two cases. In our previous work, analyses of global energy transport [2] and particle transport [3] were carried out at $R_{ax} \geqq$ 3.6 m and did not include the data at R_{ax} = 3.5 m. The data analyzed in this section are taken from those in Fig. 2. The averaged line density was kept around 1.5×10^{19} m^{-3}, and electron temperatures were scanned by changing NBI powers in order to investigate T_e dependence of transport coefficients. In this study, we focus our attention on T_e dependence of transport coefficients, because T_e strongly dictates transport irrespective of whether it is neoclassical or anomalous.

Particle transport in LHD was studied using density modulation experiments due to external periodic gas fueling, where the diffusion coefficient (D) and convection velocity (V) were determined to fit measured modulation amplitudes, phases, and background density profiles [3,4]. The modulation frequencies were 2.0, 5.0, and 10.0 Hz. Figure 5 shows models used for the fitting of D and V. When the modulation frequency is high or diffusion coefficient is small, the modulation amplitude is localized in the edge, and the analysis becomes insensitive to core diffusion. Thus, the model of spatially constant D was used as shown in Fig. 5 (a). When a modulation frequency is low
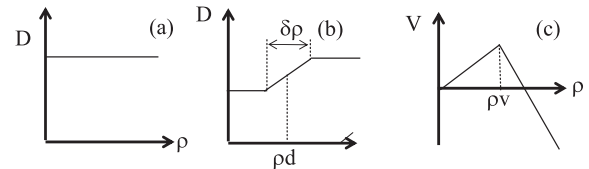

Fig. 5 Assumed spatial profiles of D and V. (a) Spatially Spatially constant D for localized modulation amplitude cases, (b) two variable D for core sensitive cases, and (c) two variable V for all cases.
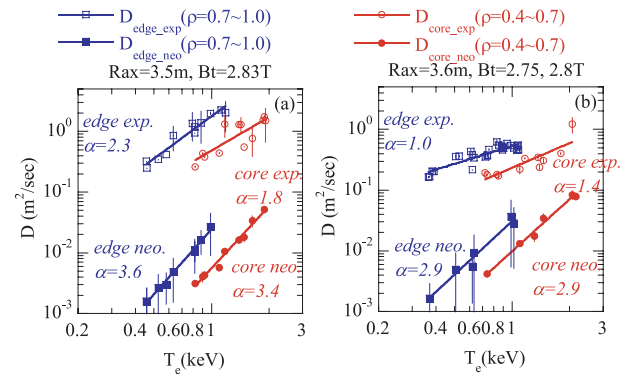

Fig. 6 Electron temperature dependence of diffusion coefficients: (a) R_{ax} = 3.5 m in B_t = 2.83 T, and (b) R_{ax} = 3.6 m in B_t = 2.75 and 2.80 T. D_{core_exp} and D_{edge_exp} are experimentally estimated core and edge diffusion coefficients. D_{core_neo} and D_{edge_neo} are neoclassical values calculated using the DCOM code. Error bars of experimental values are ranges of uncertainty for fitting to experimental data, and error bars of neoclassical values are standard deviations at ρ = 0.4-0.7 for core values, and at ρ = 0.7-1.0 for edge values. T_e was also averaged at ρ = 0.4-0.7 for core values, and at ρ = 0.7-1.0 for edge values.

or diffusion coefficient is large, modulation penetrates deep into the core. Thus, the two-parameter diffusion coefficient model was used as shown in Fig. 5 (b), where the diffusion coefficient was assumed to change at $\rho = \rho_d$ with a transition width $\delta\rho$. The convection velocity was assumed to be zero at the plasma center and to increase linearly and change a slope at $\rho = \rho_v$.

In the model shown in Fig. 5, the value of ρ_d was fixed at 0.7 for all cases. For R_{ax} = 3.5 m in B_t = 2.83 T, $\delta\rho$ was fixed at 0.6, and ρ_v was fixed at 0.5. For other configurations, when the modulation penetrated deeper to the core, $\delta\rho$ was fixed at 0.1 and ρ_v was fixed at 0.7. These values were determined a posteriori for good fitting.

Figure 6 shows the T_e dependence of D_{core} and D_{edge}. Neoclassical values calculated using the DCOM code [1] are also shown. Neoclassical values of D_{core} and D_{edge} were estimated as averages over ρ = 0.4 - 0.7 and ρ = 0.7 - 1.0, respectively. Neoclassical values of V_{core} were defined as those at ρ = 0.7. Error bars of neoclassical values of D in Fig. 6 are standard deviations over the averaged regions.

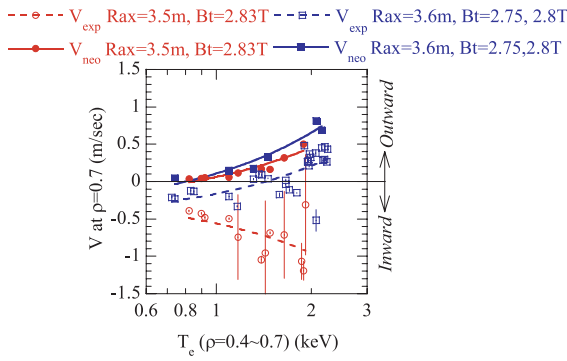On the other hand, experimental values of D_{edge}, D_{core},

Fig. 7   Dependence of V_{core} (at $\rho = 0.7$) on T_e. T_e is the averaged value at $\rho = 0.4$-0.7. V_{exp} is the experimentally estimated core convection velocity at $\rho = 0.7$. V_{neo} denotes the neoclassical values calculated using the DCOM code at $\rho = 0.7$. Error bars of experimental values are ranges of uncertainty for fitting to experimental data.

V_{edge}, and V_{core} were defined as follows: spatially constant values of D were used as D_{edge}, in case the modulation amplitude was localized in the edge region. For other cases, in the two-parameter diffusion model, D_{core} and D_{edge} were used as averaged values between $\rho = 0.4$ and 0.7 and between $\rho = 0.7$ and 1.0 respectively. Values of V_{core} were defined as those at $\rho = 0.7$.

The fitted lines in Fig. 6 are $A \times T_e^{\alpha}$, where A is a proportional factor and α is an exponent. Neoclassical values are slightly smaller at $R_{ax} = 3.5$ m than at $R_{ax} = 3.6$ m at the same values of T_e.

At both $R_{ax} = 3.5$ m and 3.6 m, the temperature exponent factor α for neoclassical diffusion is larger than that for the experimental values as shown in Figs. 6 (a) and (b). Experimentally determined values of D_{core} and D_{edge} are more than one order of magnitude larger than neoclassical values in the present experimental regime. The difference between experimental and anomalous transports was larger at $R_{ax} = 3.5$ m than at $R_{ax} = 3.6$ m. Experimentally estimated values of D_{core} and D_{edge} were larger at $R_{ax} = 3.5$ m than at $R_{ax} = 3.6$ m. In addition, temperature exponents for experimental D_{core} and D_{edge} are larger for $R_{ax} = 3.5$ m than for $R_{ax} = 3.6$ m, while those for neoclassical values are about the same. These overall observations, namely a higher degree of anomaly and higher temperature dependence of diffusion coefficients for $R_{ax} = 3.5$ m than $R_{ax} = 3.6$ m, may indicate different driving mechanism(s) for these two cases, with enhanced particle diffusion for the former.

The parameter dependence of convection velocity was studied and compared with neoclassical prediction for $R_{ax} = 3.5$ m and 3.6 m. The results are shown in Fig. 7. In Fig. 7, the lines are linear fitting lines. Here, the core convection velocity (V_{core} at $\rho = 0.7$) was summarized, because it strongly influences density profiles.

The neoclassical particle flux is given by the following

equation [14]:

$$\Gamma_{e\_neo} = -nD_1 \left\{ \frac{\nabla n_e}{n_e} + \frac{eE_r}{T_e} + \left(\frac{D_2}{D_1} - \frac{3}{2} \right) \frac{\nabla T_e}{T_e} \right\} \quad (4)$$

Since the off diagonal terms of Eq. (4) indicate convective fluxes, the neoclassical convection velocity is defined by the following equation:

$$V_{e\_neo} = -D_1 \left\{ \frac{eE_r}{T_e} + \left(\frac{D_2}{D_1} - \frac{3}{2} \right) \frac{\nabla T_e}{T_e} \right\} \quad (5)$$

From Fig. 7, the following results were obtained. As shown in Fig. 7, opposite T_e dependence of the experimental V_{core} was observed at two configurations. At $R_{ax} = 3.5$ m in $B_t = 2.83$ T, the experimental V_{core} increased inwardly with increasing T_e, while at $R_{ax} = 3.6$ m in $B_t = 2.75$ and 2.80 T, the experimental V_{core} increased outwardly with increasing T_e. The opposite T_e dependence of experimental V_{core} resulted in opposite ν_b^* dependence of the density peaking factor, as shown in Fig. 2 (a). On the other hand, at both configurations, the neoclassical V_{core} is directed outward and increased outwardly with increasing T_e.

In both cases, absolute values from the neoclassical prediction are much closer to the values determined experimentally, which is quite a different characteristic from that for diffusion coefficients.

2.3   Configuration dependence of neoclassical and anomalous particle transport coefficient

Optimized configuration for reducing anomalous transport was attempted at $R_{ax} = 3.5, 3.6, 3.75,$ and 3.9 m in $B_t = 2.54$-2.83 T. The toroidal magnetic field varied around 10 %.

Figure 8 shows the configuration dependence of D_{core}, D_{edge} and V_{core}, where the solid lines indicate neoclassically and experimentally determined values for each configuration at temperature T_e shown in each graph. Figures 8 (a) and (b) show that experimentally estimated values of D_{core} and D_{edge} have a minimum at $R_{ax} = 3.75$ m, while neoclassical values of D_{core} and D_{edge} have a minimum at $R_{ax} = 3.5$ m. Thus, different optimum configurations of particle diffusion among neoclassical and anomalous transports were found. Also, the difference is smaller in the core region than in the edge region. This indicates that anomalous transport is stronger in the edge region. This is consistent with the previous results [3], where edge fluctuation levels increased with an increase of experimentally determined values of D_{edge}.

Global particle confinement is usually dominated by edge diffusion. The best global particle confinement was achieved at $R_{ax} = 3.75$ in the experimental regime described in this article, which is not neoclassically optimized. On the other hand, the best energy confinement is achieved at $R_{ax} = 3.6$ m [2]. These results indicate that
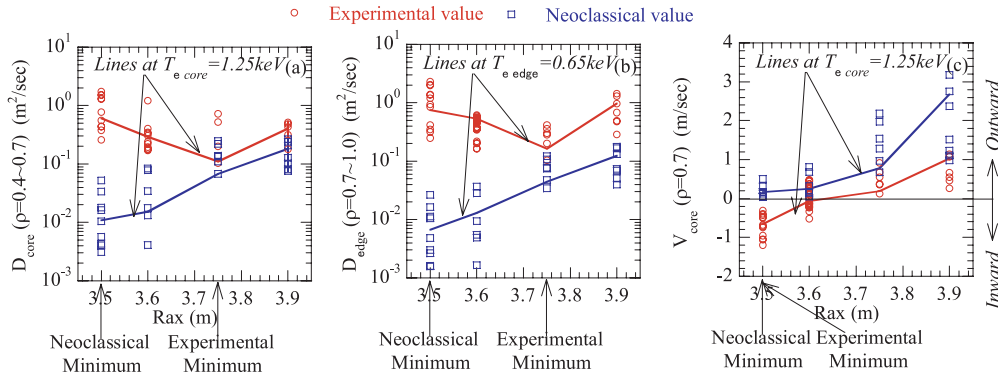
Fig. 8   Comparison between neoclassical and anomalous transport coefficients at high field (a) D_{core}, (b) D_{edge}, and (c) V_{core} at $B_t = 2.83$ T for $R_{ax} = 3.5$ m, $B_t = 2.75$ and 2.8 T for $R_{ax} = 3.6$ m, $B_t = 2.64$ T for $R_{ax} = 3.75$ m, $B_t = 2.54$ T for $R_{ax} = 3.9$ m. Red and blue lines indicate the values the same temperature.

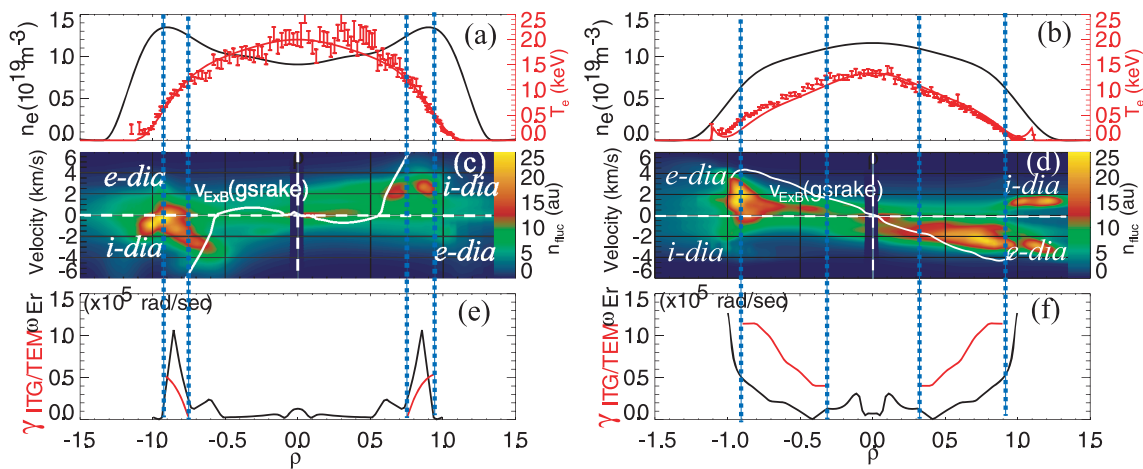Fig. 9   Comparison of (a), (b) n_e and T_e profiles and (c), (d) fluctuation amplitude profiles ($k = 0.1$-0.6 mm^{-1}) and (e), (f) ITG/TEM linear growth rates ($\gamma_{ITG/TEM}$) and E_r shearing rate rates (ωE_r). In (c) and (d), $E_r \times B_t$ poloidal rotation velocities are shown using white lines. In (e) and (f), ITG/TEM linear growth rates are shown using red lines, E_r shearing rate rates are shown using black lines. In these figures, $R_{ax} = 3.5$ m in $B_t = 1.45$ T, and (a), (c), and (e) are at a high NBI heating power (11.3 MW), while (b), (d), and (f) are at a low heating power (1.7 MW)

the minimum of energy transport is different from that of particle transport.

As shown in Fig. 8 (c), both experimentally and neoclassically determined values of V_{core} (at $\rho = 0.7$) showed a minimum at $R_{ax} = 3.5$ m and their difference does not change dramatically among configurations compared with the difference of D_{core} and D_{edge}. The higher the outwardly directed convection velocity becomes, the more hollow the density profile tends to be. The above observations from Fig. 8 (c) support measured density peaking factors shown in Fig. 4, where the more outwardly shifted configurations yield more hollow density profiles.

2.4   Possible role of turbulence on density profile

Turbulence was measured using two-dimensional phase contrast imaging (2D PCI) [16, 17]. In the previous report, edge turbulence was studied in order to find

a linkage between edge transport and edge fluctuations at $\rho \sim 1.0$ [3, 4]. Here, the magnification of 2D PCI was adjusted to look at core fluctuations at $\rho < 1.0$, with $k = 0.1$ - 0.6 m^{-1}, with good spatial resolution so that the density profiles and core turbulence can be correlated.

Figure 9 shows spatial profiles of n_e, T_e, fluctuations, linear growth rates in the ion temperature gradient and trapped electron (ITG/TEM) modes, and E_r shearing rates for the two different NBI heating powers at $R_{ax} = 3.53$ m in $B_t = 1.45$ T. The positive and negative values of ρ correspond to the upper and lower parts in the measurement-cross section, respectively. The linear growth rate was calculated by GOBLIN code [12] and the E_r shearing rate was calculated from the E_r profiles obtained from the neoclassical ambipolar condition using the GSRAKE code [15]. The NBI heating power was 11.3 MW and 1.7 MW in Figs. 9 (a), (c), and (e) and Figs. 9 (b), (d), and (f), respectively. For the former case, large Shavanov shifts were induced, resulting in the magnetic axis to be shifted at

3.63 m. For the latter case, negligible Shavanov shifts were resulted, resulting in the magnetic axis to be fixed in vacuum at 3.53 m. Therefore, the comparison in Fig. 9 indicates the difference in fluctuation character between the peaked density profile observed at R_{ax} = 3.5 m in B_t = 2.83 T and the hollow density profile observed at R_{ax} = 3.6 m in B_t = 2.75, 2.8 T.

Spatial profiles of the fluctuation amplitude are shown at each phase velocity of fluctuations. Here, the phase velocity is the velocity in the laboratory frame. Clear differences in the fluctuation amplitude are seen in Figs. 9 (c) and (d).

For hollow density profiles in the high heating power case (Figs. 9 (a), (c), and (e)), the dominant part of fluctuations are localized in the edge region (ρ = 0.8 - 1.1). The linear growth rate of the ITG/TEM modes is positive in this region, rendering them unstable, but they are stabilized by the E_r shearing rate because the E_r shearing rate exceeds the linear growth rates, as shown in Fig. 9 (e). On the other hand, for peaked density profiles at the low heating power case (Figs. 9 (b), (c), and (f)), the dominant part of fluctuations existed at the plasma center. In this region, the ITG/TEM modes are unstable, and they are not stabilized by the E_r shearing rate as shown in Fig. 9 (f). As described in Sections 2.2 and 2.3, the contribution of anomalous transport is large in determining the peaked density profiles at R_{ax} = 3.5 m in B_t = 2.83 T. Observed larger fluctuation amplitudes at peaked density profiles qualitatively agree with this fact.

3. Summary

The parameter dependence of density profiles and particle transport was studied in a wide operational regime of LHD. Two different dependences on ν_b^* of the density peaking factor were identified. Namely, the first is a gradual increase of density peaking factors with reducing ν_b^* at R_{ax} = 3.5 m in 2.83 T, where neoclassical transport is minimum among the dataset used in the analysis. This behavior is similar to that observed in many tokamaks. The other is a decrease in density peaking factors with decreasing ν_b^*. This is observed in configurations other than R_{ax} = 3.5 m and is special for LHD.

The electron temperature dependences of D and V were investigated at optimum neoclassical configuration: R_{ax} = 3.5 m in 2.83 T, and R_{ax} = 3.6 m in 2.75 T and 2.80 T. The diffusion coefficient was one order of magnitude larger than neoclassical values for both configurations. However, T_e dependence was different; that is for R_{ax} = 3.5 m in 2.83 T, the T_e dependence was stronger than that for R_{ax} = 3.6 m in 2.75 T and 2.80 T. At the neoclassically optimized configuration (R_{ax} = 3.5 m, 2.83 T), the convection velocity at ρ = 0.7 was directed inward, contrary to the prediction of the neoclassical theory. On the other hand, at R_{ax} = 3.6 m in 2.75 T and 2.80 T, the convection velocity at ρ = 0.7 was inwardly directed at lower T_e and reversed to the outward direction at higher T_e. Absolute values of the convection velocity were comparable to the neoclassical values. These observations support measured density peaking factors, where the more outwardly shifted configurations yield more hollow density profiles. Also, the present results show that the configuration of the neoclassically determined minimum condition for the diffusion coefficient is not the same as anomalously determined minimum configurations.

A difference in core turbulence was observed among hollow and peaked density profiles. This observation is consistent with the expectations of ITG/TEM, which suggest that turbulence has an influence on measured density profiles described above.

Acknowledgements

[1] S. Murakami *et al.*, Nucl. Fusion **42**, L19–L22 (2002).
[2] H. Yamada *et al.*, Nucl. Fusion **45**, 1684 (2005).
[3] K. Tanaka *et al.*, Fusion. Sci. Technol. **51**, 97 (2007).
[4] K. Tanaka *et al.*, Nucl. Fusion **46**, 110 (2006).
[5] K. Tanaka *et al.*, to be submitted J. Plasma Fusion. Res.
[6] K. Tanaka *et al.*, Plasma Fusion. Res. **2**, S1033 (2007).
[7] K. Narihara *et al.*, Rev. Sci. Instrum. **72**, 1122 (2001).
[8] H. Takenaga, K. Tanaka, K. Muraoka *et al.*, Nucl. Fusion **48**, 075004 (2008).
[9] C. Angioni *et al.*, Phys. Plasmas **10**, 3225 (2003).
[10] C.D. Beidler and W.N.G. Hitchon, Plasma Phys. Control. Fusion **36**, 317 (1994).
[11] M. Yokoyama *at al.*, J. Plasma Fusion. Res. **81**, 83 (2005).
[12] O. Yamagishi *et al.*, Phys. Plasmas **14**, 012505 (2007).
[13] H. Funaba *et al.*, J. Plasma Fusion. Res. **3**, 022 (2008).
[14] V. Tribaldos Phys. Plasmas **8**, 1229 (2001).
[15] C.D. Beidler and W.D. D'haeseleer, Plasma Phys. Control. Fusion **37**, 463 (1995).
[16] C. Michael *et al.*, Rev. Sci. Instrum. **77**, 10E923-1 (2006).
[17] C. Michael *et al.*, Plasma Fusion. Res. **2**, S1034 (2007).